

Chapter 7 |

Metastable phase study in the Ti-Ta and Ti-Nb systems

7.1 Introduction

The present chapter is aimed at studying the metastable phases ω and α'' in Ti-alloys. The first part of this work looked at the elastic properties of the metastable phases. As shown in Figures 1.1 and 1.2, the formation of the α'' and ω phases affects the elastic properties of Ti-Ta and Ti-Nb alloys. For Ti-Nb, the CALPHAD prediction shows that the alloys will form either the single hcp or bcc phases or a two-phase mixture of bcc and hcp and does not have any modeling completed for the α'' phase. The second part of this work looks at improving the thermodynamic properties to predict the probability and formation of these phases. Understanding the effect of the metastable phases on the elastic properties and being able to predict at what compositions they form, will help with alloy selection and increase the likelihood of finding a suitable alloy for load-bearing implants. The elastic properties of the four phases are calculated systematically and interaction parameters are introduced using the CALPHAD method, similar as described in chapter 5, to be able to predict the elastic properties as a function of composition. The stability of the bcc, hcp, ω , and α'' phases at 0 K is calculated and discussed for the Ti-Ta and Ti-Nb alloys using multiple structures across the entire composition range. The modeling of these four phases was then studied and in order to validate the modeling, elastic properties and transformation predicted, inelastic neutron scattering experiments were completed on 4 different Ti-Nb compositions. The data from the experiments

is used to determine the fraction of phases and phonon density of phases. The results from the neutron scattering were compared with the theoretical results.

7.2 Modeling and Calculations

In the present work, the Vienna ab-initio Simulation Package (VASP) [61] was employed to calculate the ground state energy and elastic properties of the pure elements and Ti-Nb and Ti-Ta systems in the bcc, hcp, ω , and α'' phases. The ion-electron interactions were described using the projector augmented wave (PAW) [62, 89] method and based on the previous work of comparing X-C functionals (Figure 5.1) the exchange-correlation functional of the generalized gradient approach depicted by Perdew, Burke, and Ernzerhof (PBE-GGA) was employed [58]. The energy convergence criterion of the electronic self-consistency was set as 10^{-6} eV/atom. Independent structures based on the ATAT code were generated for the four phases, bcc (330), hcp (21), α'' (33) and ω (73), across the entire composition range. The Brillouin zone sampling was done using the Γ -centered Monkhorst-Pack scheme [90]. The k-points grid for the hcp, ω and α'' phases were 10x10x13, 13x13x7, and 12x11x10, respectively. The k-point grids for the bcc calculations used the automated k-point mesh generator in VASP with the length of the subdivisions specified as 50. The elastic properties were then calculated using a ± 0.01 magnitude of strain.

The elastic stiffness coefficients were modeled using the results from the DFT-based first-principles calculations. The modeling was completed by the methodology outlined in chapter 2. The difference between the first-principles calculations and the linear combination from the pure elements was calculated and the fittings were completed using the code in appendix C. The best fit was found by comparing one interaction parameter or two interaction parameters. The moduli values were then calculated using pycalphad and the code in appendix D and E [42].

7.3 Results and discussion

7.3.1 Elastic properties

For the Ti-Nb system, the elastic stiffness coefficients of the bcc, hcp, α'' , and ω phases are calculated. The calculations and interaction parameters of the bcc phase are discussed in chapter 5. Figure 7.4 and 7.5 plot the elastic stiffness coefficients, c_{11} , c_{12} , c_{13} , c_{22} , c_{23} , c_{33} , c_{44} , c_{55} , and c_{66} , for the α'' phase. The plots show the first-principles results (circles), the linear combination from the pure elements (dashed red line) and the modeling prediction (solid line) using the interaction parameters in Table 7.1. Figure 7.4 shows a negative deviation from Vegard's law for the c_{11} , c_{22} and c_{33} elastic stiffness coefficients [125]. The c_{12} values show a positive deviation from Vegard's law while the c_{13} values show a positive deviation until approximately 50 at. % Nb when the values show a negative deviation from Vegard's law. Figure 7.5 shows that the c_{33} and c_{66} values have a negative deviation from Vegard's law. The c_{55} values show a negative deviation from Vegard's law until around 30 at. % Nb when the values begin to positively deviate. The c_{44} values show no deviation from Vegard's law [125].

Figure 7.6 plots the elastic stiffness coefficients, c_{11} , c_{12} , c_{13} , c_{33} , and c_{44} , for the ω state. The plots show the first-principles results (circles), the linear combination from the pure elements (dashed red line) and the fitting (solid line) using the interaction parameters in Table 7.1. The c_{11} and c_{12} values show a negative deviation from Vegard's law while the c_{13} values show a positive deviation [125]. The c_{33} and c_{44} values show a negative deviation to start and then a positive deviation from Vegard's law.

Figure 7.7 plots the elastic stiffness coefficients, c_{11} , c_{12} , c_{13} , c_{33} , and c_{44} , for the hcp state. The plots show the first-principles results (circles), the linear combination from the pure elements (dashed red line) and the fitting (solid line) using the interaction parameters in Table 7.1. The c_{11} values show a slight positive deviation and then a large negative deviation from Vegard's law while the c_{12} and c_{13} values show a negative deviation and then positive deviation from Vegard's law [125]. The c_{33} and c_{44} values show a negative deviation from Vegard's law.

The interaction parameters determined are listed in 7.1 and the calculated elastic stiffness coefficients and E values are listed in Table 7.2. The Young's

moduli values are calculated as a function of composition and are plotted in Figure 7.8. The dotted lines are the modeling predictions calculated from the interaction parameters in Table 7.1. The calculations show that the Young's moduli for the hcp state decrease (in value) from pure Ti (124 GPa) to pure Nb (-158 GPa). The Young's moduli, for the ω state, follows a somewhat similar trend as the hcp state. The E values, for the ω state, decrease from pure Ti (152 GPa) to -163 GPa at 60 at. % Nb and then increase to 162 GPa at pure Nb. The E values for the bcc state increase from -40 GPa at pure Ti to 98 GPa at pure Nb. The E values for the α'' state decrease from 133 GPa at pure Ti to 82 GPa at 30 at. % Nb, then increase to 123 GPa at 80 at. % Nb and then decrease to 90 GPa at pure Nb. The E values for the hcp, ω , and bcc states all become negative at certain compositions. Based on Born's criteria, a negative Young's modulus can indicate that the state is not stable at that composition. From Figure 7.8 it can be seen that the E values of the α'' state are higher than the E values of the hcp or bcc states. This explains why the experimental Young's moduli increase in value with the formation of α , as seen in Figure 1.2.

Different authors experimentally determined the E of various Ti-Nb alloys at different compositions, as seen in Figure 1.2, [6, 8, 8, 9]. Ozaki et al. [7] showed that at certain compositions quenched Ti-Nb samples formed bcc and α'' while the slow cooled samples formed bcc and ω . For the quenched samples, there is more data available in the literature [6, 8, 8, 9], and therefore the present work averaged the E values obtained by different researchers for the same compositions. A full review of the experimental results is listed in appendix F and the averaged experimental values are listed in Table 7.3. From these experiments, some of the phase fractions were determined [8] and those phase fractions are listed in Table 7.3. For the compositions where the phase fractions were not determined, an extrapolation using the known phase fractions to estimate the remaining phase fractions at each composition. Those estimated phase fractions are differentiated from the experimentally determined phase fractions by labeling them with a *. Then, the rule of mixtures was used as a beginning estimate of the Young's moduli values based on these phase fractions and the interaction parameters in Table 7.1. The rule of mixtures is expressed by:

$$E_c = x_{p1}E_{p1} + x_{p2}E_{p2} \quad (7.1)$$

where x_{p1} and x_{p2} are the fractions of phase 1 and phase 2 and E_{p1} and E_{p2} are the E in phase 1 and phase 2, respectively. Based on the observations in the literature [6, 8, 8, 9], from pure Ti to 10 at. % Nb the samples are 100 % hcp and the predicted E vary, on average, from the experimental E by 3 GPa (Table 7.3). From 10 at. % Nb to 30 at. % Nb, the hcp phase is repressed and the α'' and bcc phases formed. The exact fraction of the bcc phase was measured by Friak et al. [8] for samples with 10, 20, 25, and 30 at. % Nb. An extrapolation from these values is used to estimate the fractions of the phases of the remaining alloy compositions, in this composition range. Using the phase fractions and rule of mixtures, the predicted E vary, on average, from the experimental E by 0.52 GPa. This is significantly more accurate than the 22 GPa error between the experimental and predicted E using the bcc and hcp mixture, shown in Table 7.3. Above 33 at. % Nb the samples consist of the single bcc phase. The predicted E vary, on average, by 7 GPa from the experimental E (Table 7.3). Overall, the variances are small when compared to the variances in the experiments. As seen in appendix F, the experimental E values of pure Ti in the hcp phase vary by 24 GPa. The variance between the predicted E and experimental E can be partially attributed to the fact that the predicted E are at 0 K and the experimental E are measured at 300 K. It is evident that the database can be used with the rule of mixtures to accurately predict the elastic properties of Ti-Nb alloys if the phase fraction of the metastable phases can be predicted.

7.3.2 First-principles calculations at 0 K

With the elastic properties database accurate, the attention turned to improving the modeling predictions of the four phases. The formation energy of the phases at 0 K is calculated as a function of composition for the Ti-Nb and Ti-Ta systems. Figure 7.1 and 7.2 show the formation energy of the bcc, hcp, ω , and α'' phases from 100 at. % Ti to 100 at. % Nb or Ta at 0 K. The formation energies are calculated according to Eq. 2.7 using the ground state energies of the pure elements in the SER state as reference. More calculations in the bcc phase are being completed for the Ti-Nb system. The figures show that the formation energy of the hcp phase starts at 0 at pure Ti and then increases to 28 kJ/mol-atom at pure Nb or 27 kJ/mol-atom at pure Ta. The bcc phase starts with a higher formation energy at

pure Ti (10 kJ/mol-atom) and then decreases to 0 kJ/mol-atom at pure Nb or Ta. The hcp phase is lower formation energy to 30 at. % Nb or Ta when the bcc phase has a lower formation energy. The ω and α'' have similar formation energies to the hcp phase from pure Ti to 30 at. % Nb and Ta and then some of the structures continue to have similar formation energies to the bcc phase from 30 at. % Nb or Ta to 80 at. % Nb or Ta.

Kim et al. [126] experimentally determined martensitic transformation temperature for Ti-Nb alloys between 20 and 30 at. % Nb, which is plotted on the phase diagram shown in Figure 7.3. The modeling of the ω phase has been completed but the α'' phase has not been modeled. The calculations of the finite temperature properties are going to be used to model the four phases for the Ti-Nb system. The partition function approach, methodology in appendix F, is being studied to predict the probability that the phases form and to more accurately predict the finite temperature properties of the bcc phase which is theorized to be a combination of multiple states.

7.3.3 Neutron scattering results

7.3.3.1 Phonon density of states at 300 K

In order to study the phase fractions, elastic properties and transformations occurring, four Ti-Nb alloys were measured using the ARCS neutron scattering instrument at the Spallation Neutron Source, Oak Ridge National Laboratory. As discussed in the methodology, two sets of samples were made. Each set contains a Ti-Nb alloy at the following compositions: 10, 12, 18, 20 at. % Nb. The two sets of samples were annealed at 1273 K for 24 hours. One set of samples was quenched in cold water to form the bcc and α'' phases while the second set of samples was slow cooled to form the bcc and ω phases. The neutron scattering was completed at 300 K.

In Figure 7.9, 7.10, 7.11, 7.12 the phonon density of states (DOS) at 300 K is plotted for each sample. The samples at the same compositions are plotted on the same figure for comparison. The phonon DOS of the slow cooled samples are plotted as dashed lines and the phonon DOS of the quenched samples are plotted as solid lines. It can be seen that the quenched samples show different phonon DOS compared with the slow cooled samples, which means that the samples have

different phases. In order to investigate the difference of the phonon DOS further the entropy of each sample is calculated from the phonon DOS ($Z(\varrho)$):

$$S_{vib} = 3k_B \int_0^{E_{max}} [(n+1) \ln(n+1) - n \ln(n)] Z(\varrho) dZ \quad (7.2)$$

where n is the Bose-Einstein occupation factor [127]. The entropy difference between the alloys at the same compositions is plotted in 7.13. The figure shows that the entropy difference is less than 0.02 kB/atom between the two 10 at. % Nb samples. The entropy difference then increases to less than 0.03 between the two 12 at. % Nb samples and less than 0.06 between the two 18 at. % Nb samples. Finally, the entropy difference between the two 20 at. % Nb samples reaches a peak close to 0.1 kB/atom. This would result in a 30 kB/atom free energy difference between the samples. Further investigations on these samples are necessary to understand and explain this observation.

7.3.3.2 Diffraction patterns at 300 K

The diffraction patterns for each alloy are plotted in Figure 7.14, 7.15, 7.16, and 7.17. The slow cooled samples are plotted as solid lines and the quenched samples are plotted as dashed lines. The diffraction patterns plot the intensity vs. momenta (Q). The plots are compared with diffraction patterns of Ti and Nb in the four phases from the literature to determine an approximation of the phase fractions, which are listed in Table 7.4. It can be seen that the fractions of the bcc phase of the quenched samples are 0.12, 0.20, 0.57 and 0.70 for the samples containing 10, 12, 18 and 20 at. % Nb, respectively. The slow cooled samples showed a fraction of the bcc phase of 0.2, 0.3, 0.6, and 0.7 for the samples containing 10, 12, 18, and 20 at. % Nb, respectively. The phase fractions of the quenched samples with 10 and 20 at. % Nb compare well with the fractions determined by Friak et al. [8], as shown in Table 7.3.

To further understand the formation of phases in Ti-Nb alloys the temperature dependence of these alloys will be studied by neutron scattering experiments at 500, 900 and 1110 K. The temperature dependence of the phonon DOS will provide information about the type of transformation taking place.

7.4 Conclusion

The present study systematically calculated the elastic stiffness coefficients and Young's moduli of the Ti-Nb system in the bcc, hcp, ω , and α'' phases. The general CALPHAD modeling approach was used to fit binary interaction parameters. The E values were similar for the hcp and ω phases, which is reasonable since they both have hexagonal symmetry. The α'' phase has E values that were higher than the other three phases which explains why the E increases when the α'' phase forms. Experiments showed that up to 10 at. % Nb the samples formed solely the hcp phase and the database predicted the E values by an average variance of 3 GPa from the experimental E . The samples from 10 at. % Nb to 30 at. % Nb formed the bcc and α'' or ω phases. If the samples were slow cooled they form the bcc and ω phases. If the samples were quenched they form the bcc and α'' phases. Using experimentally determined phase fractions and the rule of mixtures, the database accurately predicted the E values by an average variance of 0.52 GPa when compared with the experimental E values. At Nb concentrations greater than 30 at. % Nb samples form solely the bcc phase and the database predicted the E values by an average variance of 7 GPa from the experimental E values. The phonon DOS of the slow cooled samples and ~~the phonon DOS of~~ the quenched samples were plotted together for the same compositions and showed differences that were expected for the samples having different phases. This difference was also seen when looking at the entropy difference between the two samples. The entropy difference between the quenched and slow cooled samples increased from 10 at. % Nb to 20 at. % Nb. This increase in entropy difference must be investigated further in order to understand this observation. Using the diffraction patterns, the phase fractions in each sample were approximated. The future work will include determining the elasticity of the four Ti-Nb alloy samples made and compare it to the elastic database predictions. The temperature dependence of the phonon DOS will be completed to understand the effects on the bcc phase close to the transformation. The results from the DFT-based first-principles calculations will be used to accurately model the four phases. The partition function approach will be used to more accurately model the finite temperature properties of the bcc phase and to predict the probability of the metastable phase formation.

Table 7.1: Evaluated interaction parameters L_0 and L_1 , using Eq. 2.32, for the elastic stiffness coefficients of the hcp, α'' and ω phases in the Ti-Nb systems.

Alloy	Interaction Parameter	α''	hcp	ω
c_{11}	L_0	-102.443	-298.443	-142.979
	L_1	606.748	-588.702	159.767
c_{12}	L_0	97.3105	-45.4449	-888.25
	L_1	-186.214	224.369	-1074.08
c_{13}	L_0	-11.5368	143.819	349.337
	L_1	-307.745	250.29	275.297
c_{22}	L_0	-100.063	N/A	N/A
	L_1	355.649	N/A	N/A
c_{23}	L_0	-75.1048	N/A	N/A
	L_1	283.22	N/A	N/A
c_{33}	L_0	-468.983	-143.313	-100.909
	L_1	-114.152	-77.5489	733.448
c_{44}	L_0	14.125	-43.0296	263.258
	L_1	-	-91.4667	475.336
c_{55}	L_0	204.71	N/A	N/A
	L_1	479.179	N/A	N/A
c_{66}	L_0	-59.1357	N/A	N/A
	L_1	139.625	N/A	N/A

Table 7.2: Results of the first-principles calculations of the elastic stiffness coefficients in GPa for different atomic percent compositions in the α'' , bcc, hcp, and ω phases in the Ti-Nb system at 0 K.

$\text{Ti}_{1-b}\text{Nb}_b$	c_{11}	c_{12}	c_{13}	c_{22}	c_{23}	c_{33}	c_{44}	c_{55}	c_{66}
α''									
Ti	198	69	84	197	84	189	40	40	63
$\text{Ti}_{0.97}\text{Nb}_{0.03}$	106	112	123	152	45	138	25	17	38
$\text{Ti}_{0.87}\text{Nb}_{0.13}$	171	88	105	171	67	170	47	13	43
$\text{Ti}_{0.06}\text{Nb}_{0.94}$	307	94	119	248	143	214	31	-24	13
$\text{Ti}_{0.03}\text{Nb}_{0.97}$	307	88	115	232	124	284	59	-58	8
$\text{Ti}_{0.02}\text{Nb}_{0.98}$	293	88	115	232	124	284	59	-58	8
Nb	306	88	125	240	135	284	47	-69	9
bcc									
Ti	93	115	-	-	-	-	41	-	-
$\text{Ti}_{0.98}\text{Nb}_{0.02}$	93	115	-	-	-	-	35	-	-
$\text{Ti}_{0.87}\text{Nb}_{0.13}$	116	116	-	-	-	-	37	-	-
$\text{Ti}_{0.75}\text{Nb}_{0.25}$	140	116	-	-	-	-	34	-	-
$\text{Ti}_{0.50}\text{Nb}_{0.50}$	181	121	-	-	-	-	31	-	-
$\text{Ti}_{0.25}\text{Nb}_{0.75}$	208	130	-	-	-	-	15	-	-
$\text{Ti}_{0.06}\text{Nb}_{0.94}$	242	134	-	-	-	-	18	-	-
$\text{Ti}_{0.02}\text{Nb}_{0.98}$	242	134	-	-	-	-	18	-	-
Nb	245	144	-	-	-	-	27	-	-
hcp									
Ti	175	88	80	-	-	190	41	-	-
$\text{Ti}_{0.98}\text{Nb}_{0.02}$	79	-44	-38	-	-	73	45	-	-
$\text{Ti}_{0.75}\text{Nb}_{0.25}$	156	113	104	-	-	200	13	-	-
$\text{Ti}_{0.50}\text{Nb}_{0.50}$	124	151	135	-	-	185	-19	-	-
$\text{Ti}_{0.25}\text{Nb}_{0.75}$	76	213	156	-	-	173	-61	-	-
$\text{Ti}_{0.06}\text{Nb}_{0.94}$	15	289	177	-	-	163	-104	-	-
$\text{Ti}_{0.02}\text{Nb}_{0.98}$	34	280	185	-	-	145	-106	-	-
Nb	24	18	11	-	-	25	-6	-	-
ω									
Ti	194	87	61	-	-	246	54	-	-

Table 7.2: Results of the first-principles calculations of the elastic stiffness coefficients in GPa for different atomic percent compositions in the α'' , bcc, hcp, and ω phases in the Ti-Nb system at 0 K.

$\text{Ti}_{1-b}\text{Nb}_b$	c_{11}	c_{12}	c_{13}	c_{22}	c_{23}	c_{33}	c_{44}	c_{55}	c_{66}
$\text{Ti}_{0.98}\text{Nb}_{0.02}$	187	87	63	-	-	250	50	-	-
$\text{Ti}_{0.87}\text{Nb}_{0.13}$	171	89	83	-	-	165	30	-	-
$\text{Ti}_{0.06}\text{Nb}_{0.94}$	240	90	142	-	-	234	-22	-	-
$\text{Ti}_{0.02}\text{Nb}_{0.98}$	242	88	120	-	-	270	-5	-	-
Nb	243	181	110	-	-	212	-55	-	-

Table 7.3: Phase fractions and experimentally determined E (averaged from the data in appendix F [6, 8, 8, 9]) compared with the predicted E using the rule of mixtures and interaction parameters in Table 7.1 for the Ti-Nb system. The * denotes the estimated phase fractions as opposed to the experimentally determined phase fractions with no *.

x(Nb)	Phase Fraction	Expt E	Calc E
0.00	all hcp	118.31	123.8
0.01	all hcp	112.52	115.9
0.02	all hcp	108.33	108.8
0.05	all hcp	79.47	88.2
0.08	all hcp	66.41	69.9
0.09	all hcp	68.73	64.3
0.10	0.06 BCC/0.94 α''	84.64	95.89
0.11	0.15 BCC/0.85 α''^*	78.72	88.19
0.18	0.45 BCC/0.55 α''^*	93.02	70.08
0.19	0.49 BCC/0.51 α''^*	64.26	68.65
0.20	0.60 BCC/0.40 α''	77.62	65.74
0.22	0.63 BCC/0.37 α''^*	70.90	67.44
0.23	0.67 BCC/0.33 α''^*	75.85	67.00
0.24	0.71 BCC/0.29 α''^*	61.11	66.63
0.25	0.81 BCC/0.19 α''	72.52	66.10
0.26	0.80 BCC/0.20 α''^*	66.61	66.23
0.27	0.84 BCC/0.16 α''^*	54.61	66.98
0.29	0.91 BCC/0.09 α''^*	62.13	66.16
0.30	0.90 BCC/0.10 α''	68.11	68.21
0.34	all bcc	77.47	66.69
0.36	all bcc	73.78	69.00
0.39	all bcc	76.62	69.81
0.43	all bcc	84.05	69.77

Table 7.4: Phase fractions determined from the diffraction patterns for the Ti-Nb alloys.

Alloy	x(Nb)	Phase Fraction		
		bcc	ω	α''
Quenched	0.10	0.12	-	0.88
	0.12	0.20	-	0.80
	0.18	0.57	-	0.43
	0.20	0.70	-	0.30
Slow Cooled	0.10	0.20	0.80	-
	0.12	0.30	0.70	-
	0.18	0.60	0.40	-
	0.20	0.70	0.30	-

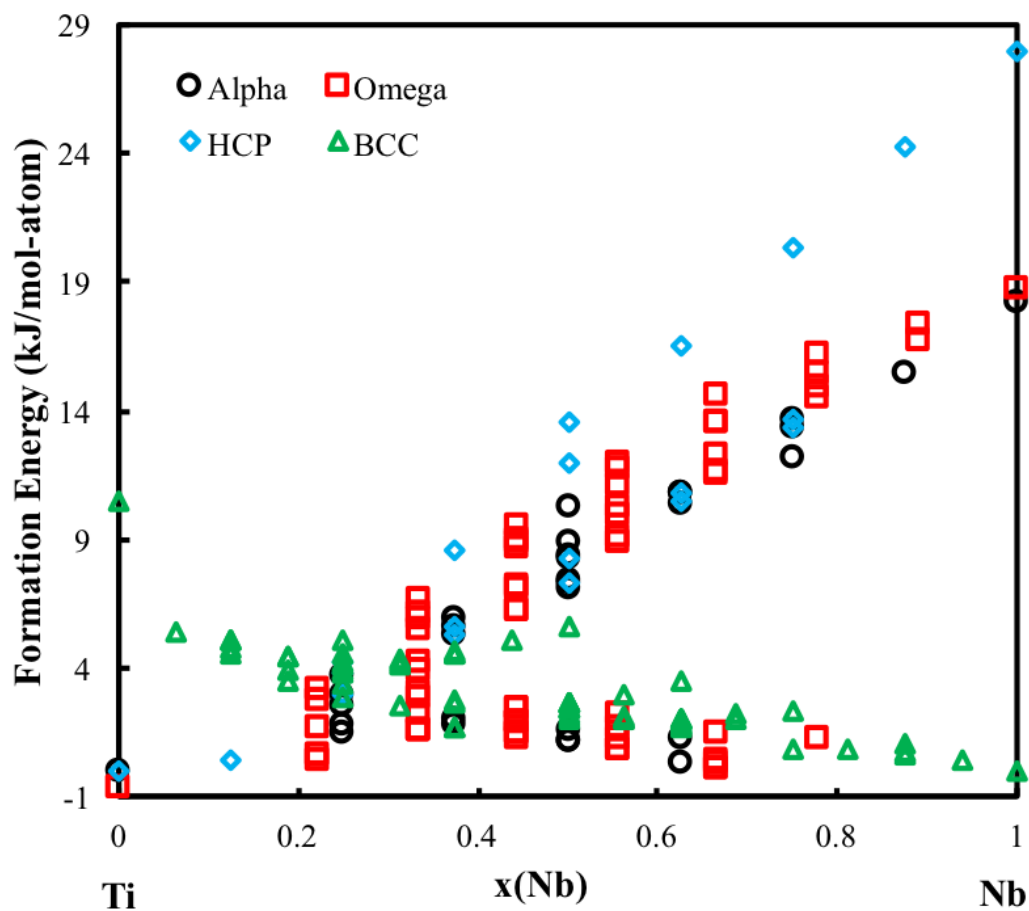


Figure 7.1: Formation energies of the bcc, hcp, ω , α'' phases in the Ti-Nb system are plotted from pure Ti to pure Nb.

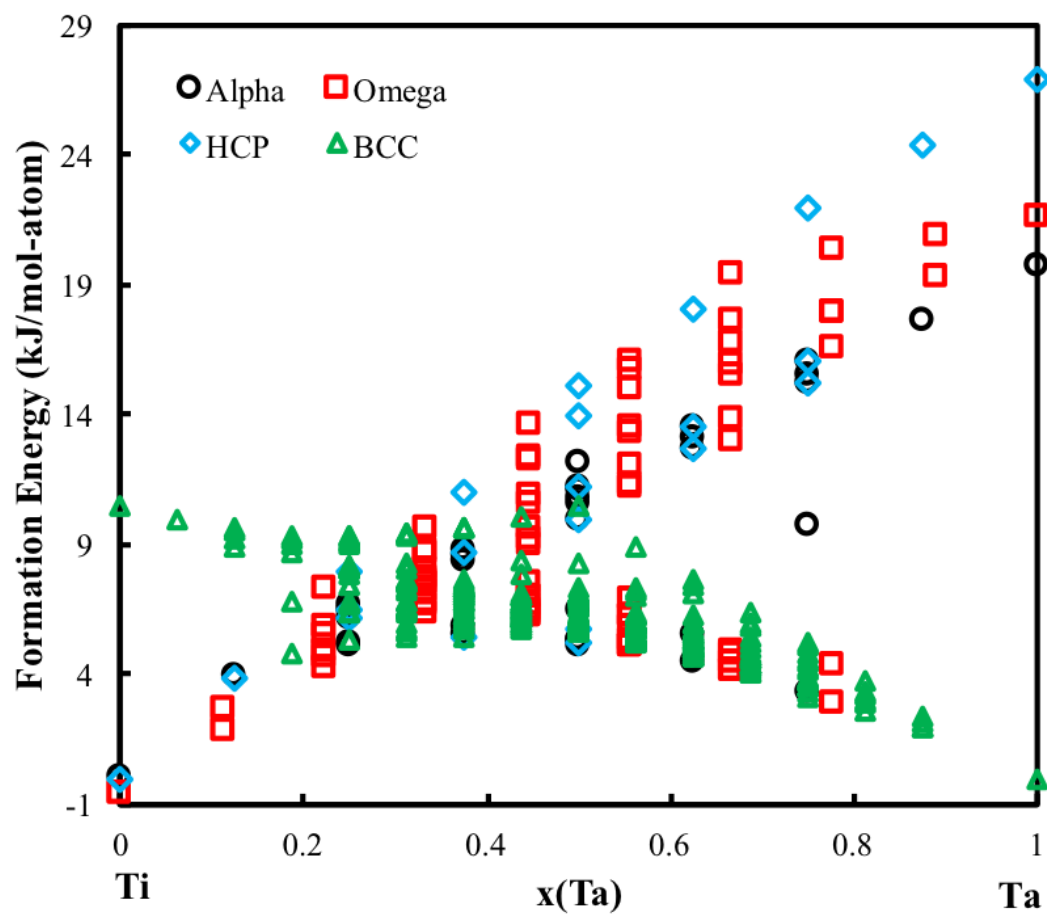


Figure 7.2: Formation energies of the bcc, hcp, ω , α'' phases in the Ti-Ta system are plotted from pure Ti to pure Ta.

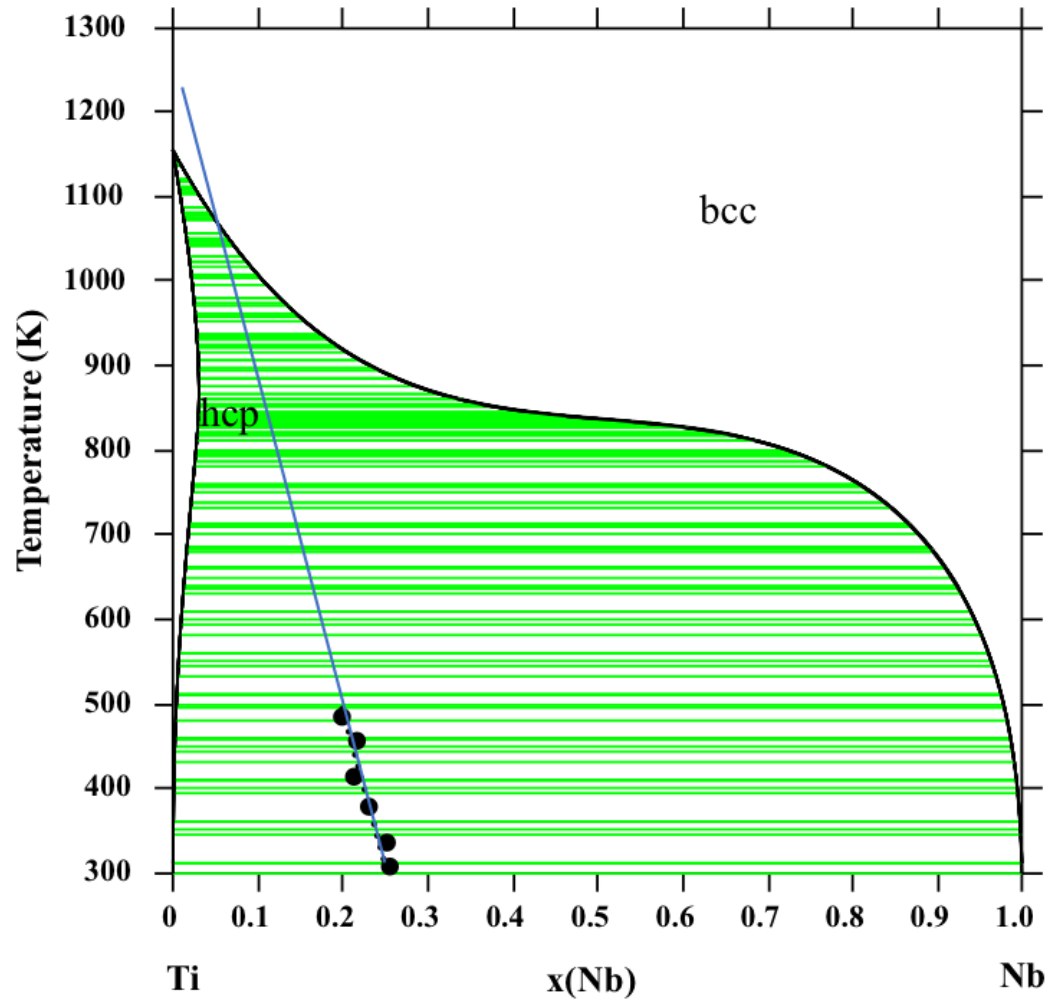


Figure 7.3: Martensitic transformation temperature is plotted versus the Ti-Nb composition.

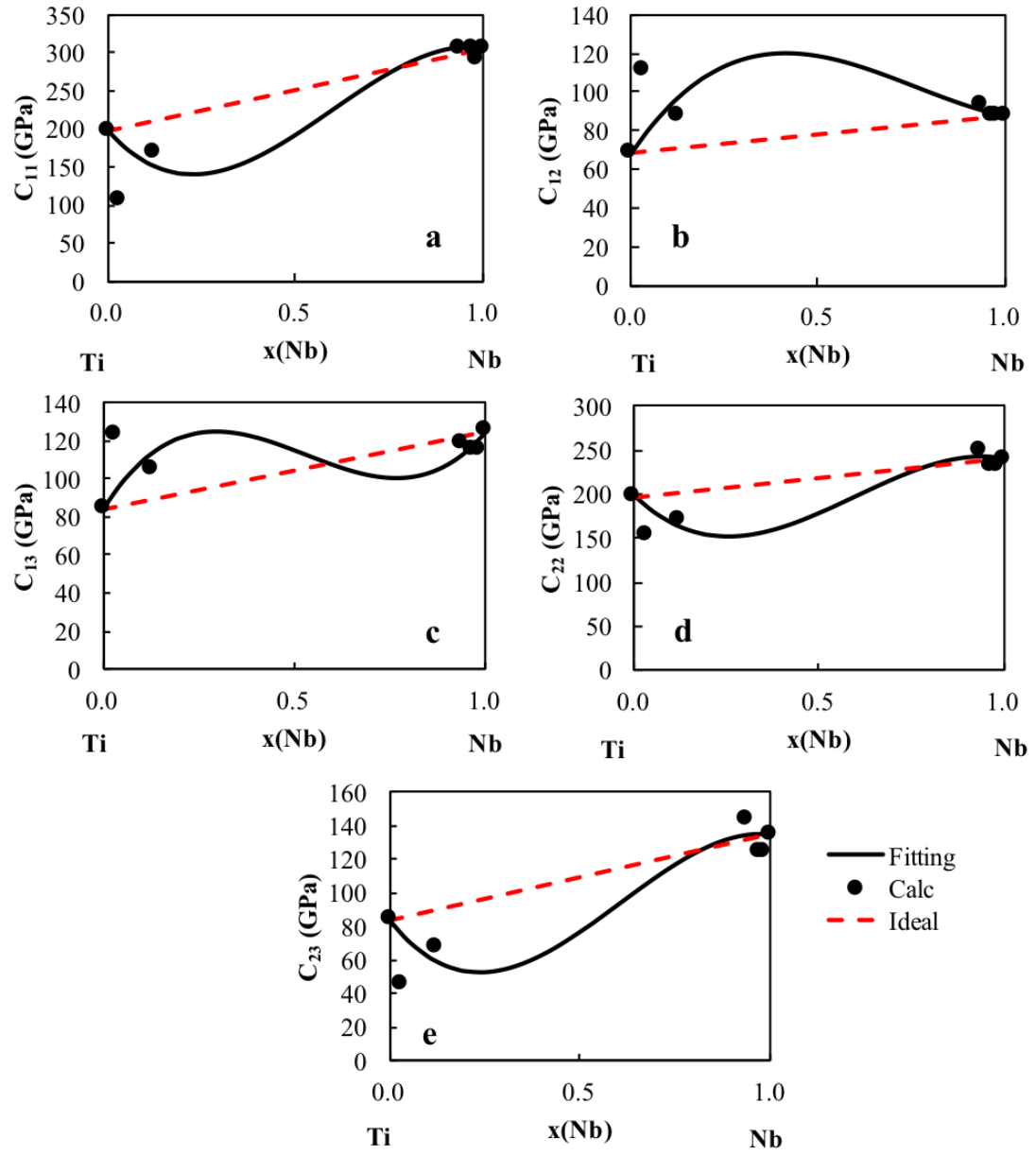


Figure 7.4: Calculated c_{11} , c_{12} , c_{13} , c_{22} , and c_{23} values (circles) plotted with the linear combination of the pure elements (red dashed line) and the present modeling (black solid line) for five of the elastic stiffness coefficients of Ti-Nb in the α'' phase.

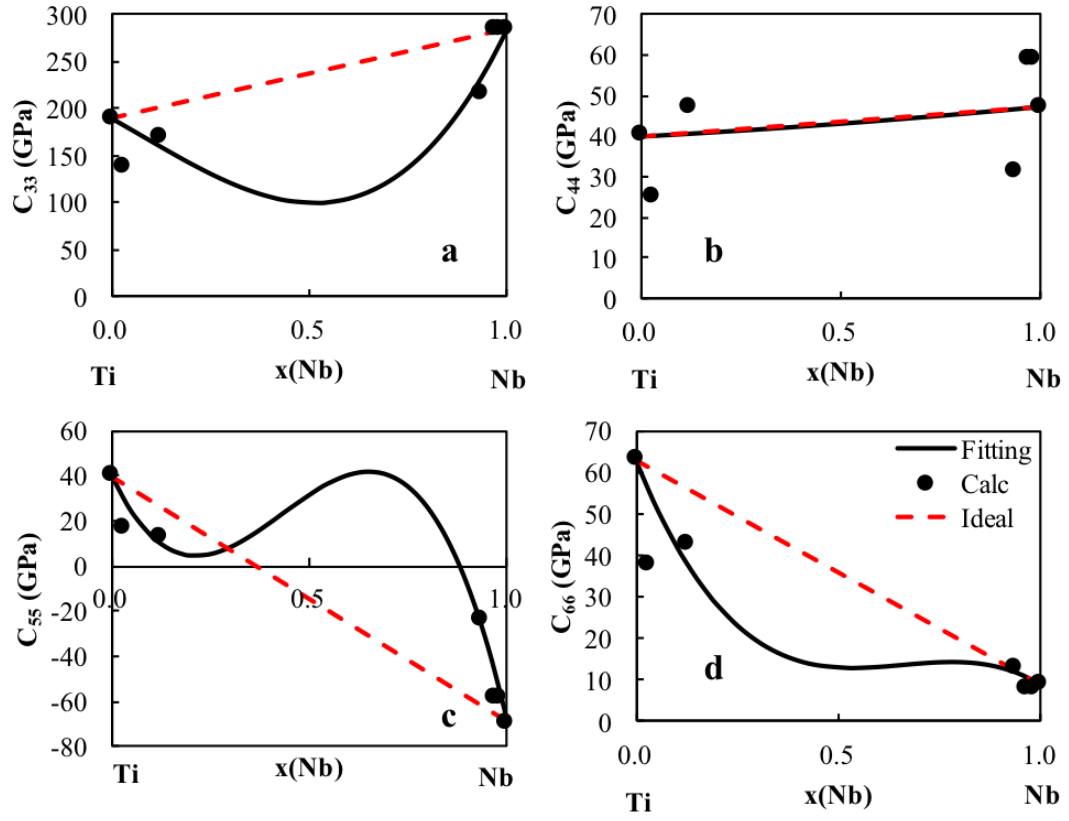


Figure 7.5: Calculated c_{33} , c_{44} , c_{55} , and c_{66} values (circles) plotted with the linear combination of the pure elements (red dashed line) and the present modeling (black solid line) for four of the elastic stiffness coefficients of Ti-Nb in the α'' phase.

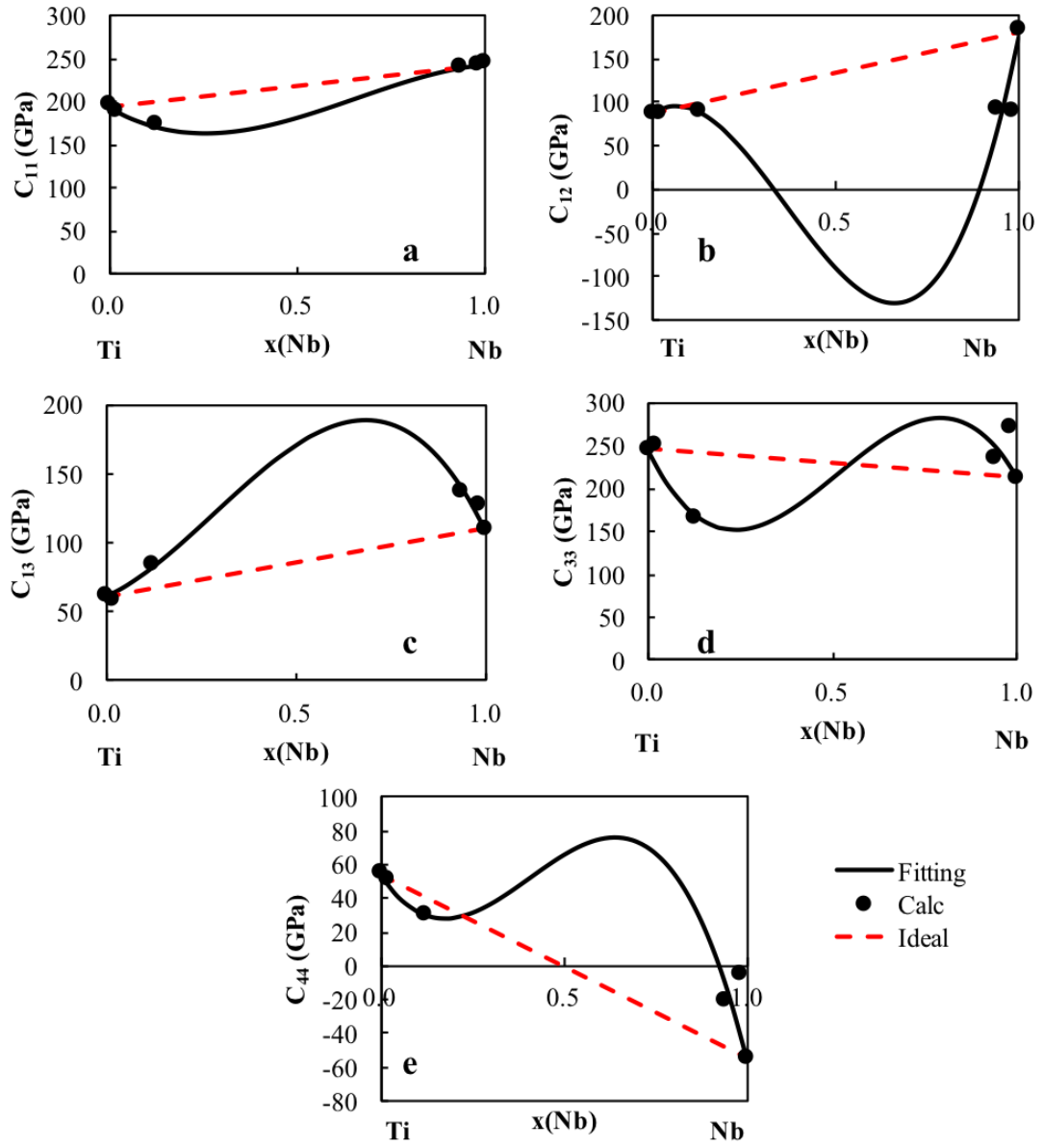


Figure 7.6: Calculated c_{11} , c_{12} , c_{13} , c_{33} , and c_{44} values (circles) plotted with the linear combination of the pure elements (red dashed line) and the present modeling (black solid line) for the elastic stiffness coefficients of Ti-Nb in the ω phase.

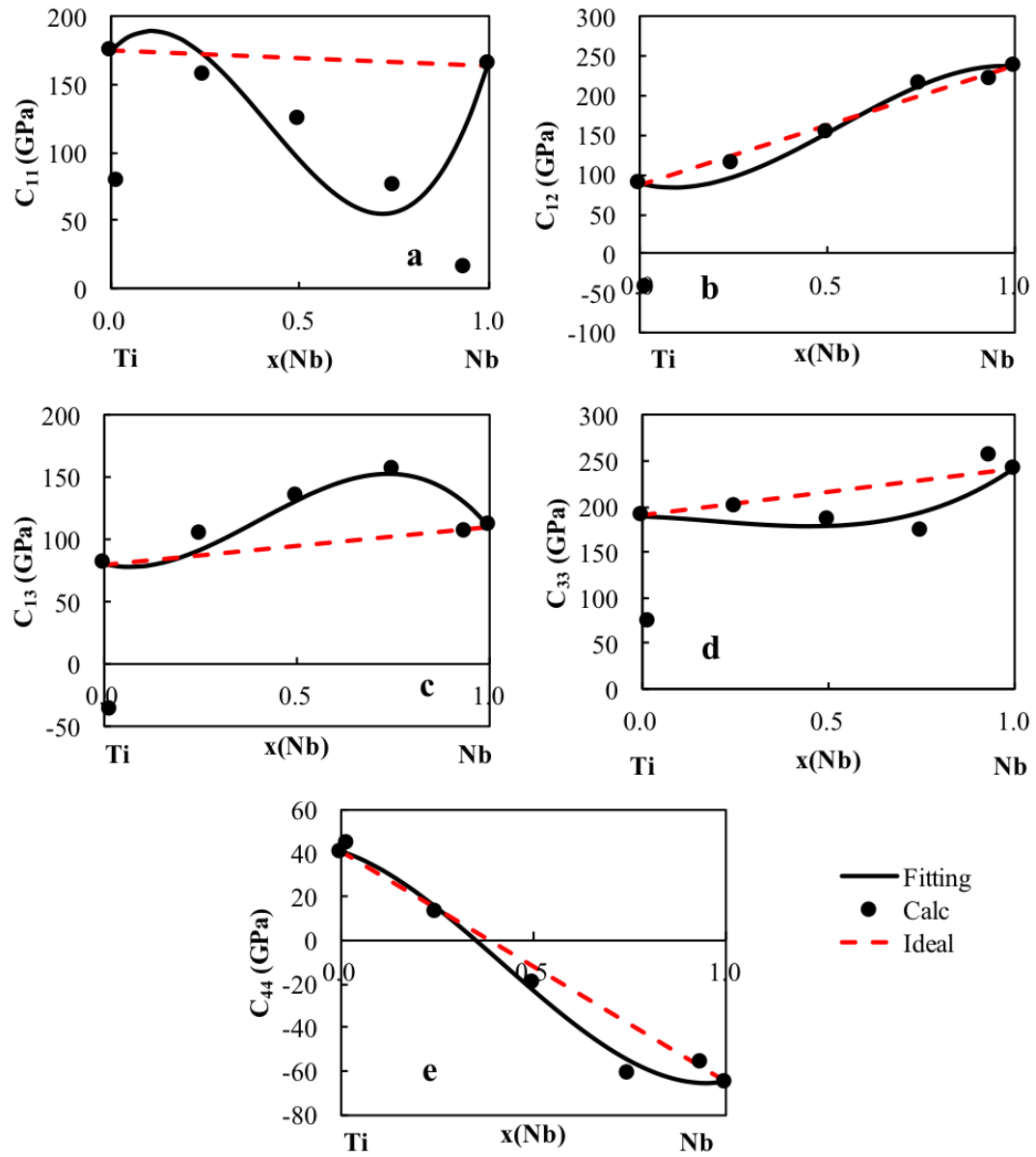


Figure 7.7: Calculated c_{11} , c_{12} , c_{13} , c_{33} , and c_{44} values (circles) plotted with the linear combination of the pure elements (red dashed line) and the present modeling (black solid line) for the elastic stiffness coefficients of Ti-Nb in the hcp phase.

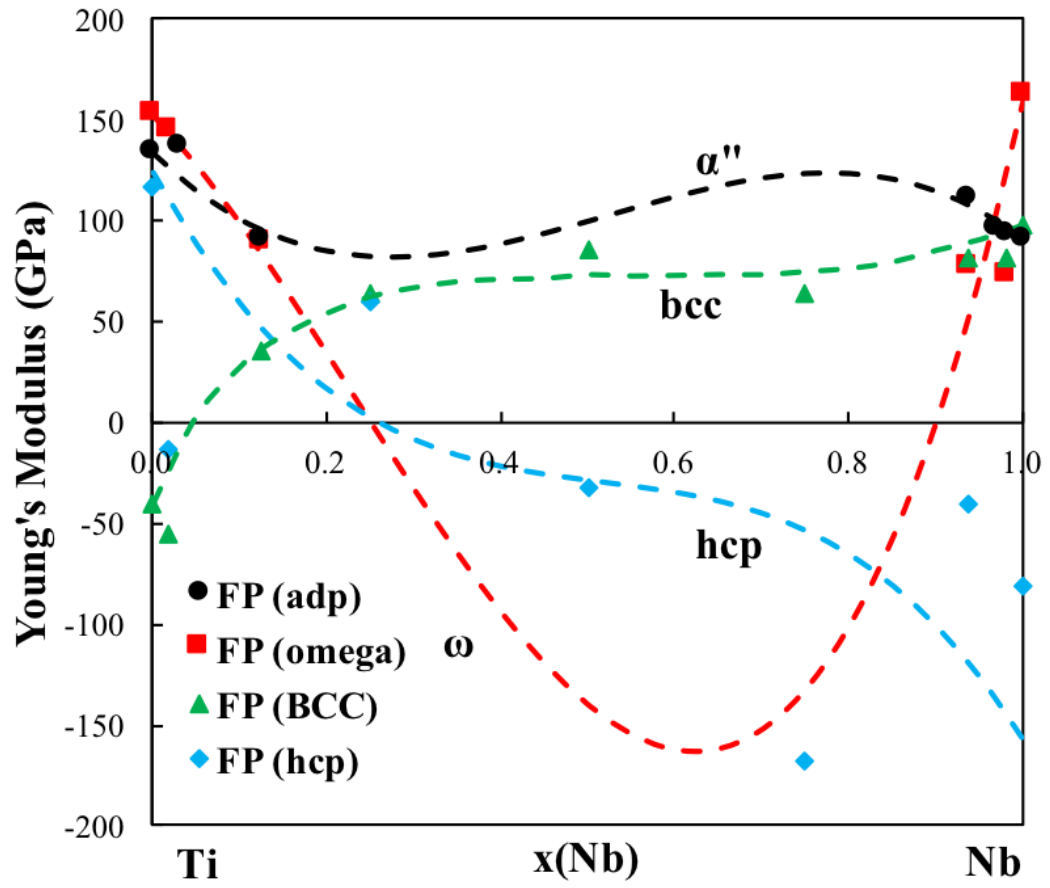


Figure 7.8: Elastic properties of the bcc, hcp, ω , α'' phases in the Ti-Nb system calculated from first-principles based on DFT are plotted as symbols. The CALPHAD fittings are plotted as the dashed lines. The figure is plotted from pure Ti to pure Nb.

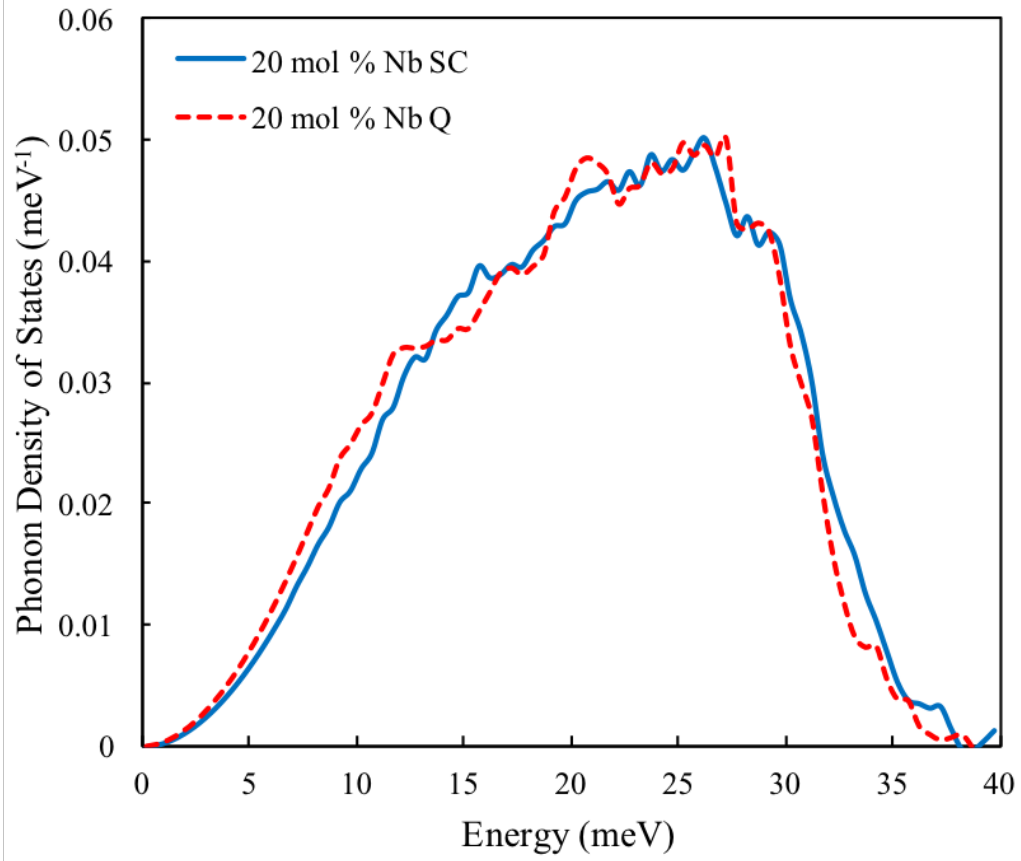


Figure 7.9: Phonon density of states for the Ti-Nb alloy at 20 at. % Nb. The dashed line represents the slow cooled sample while the solid line represents the quenched sample.

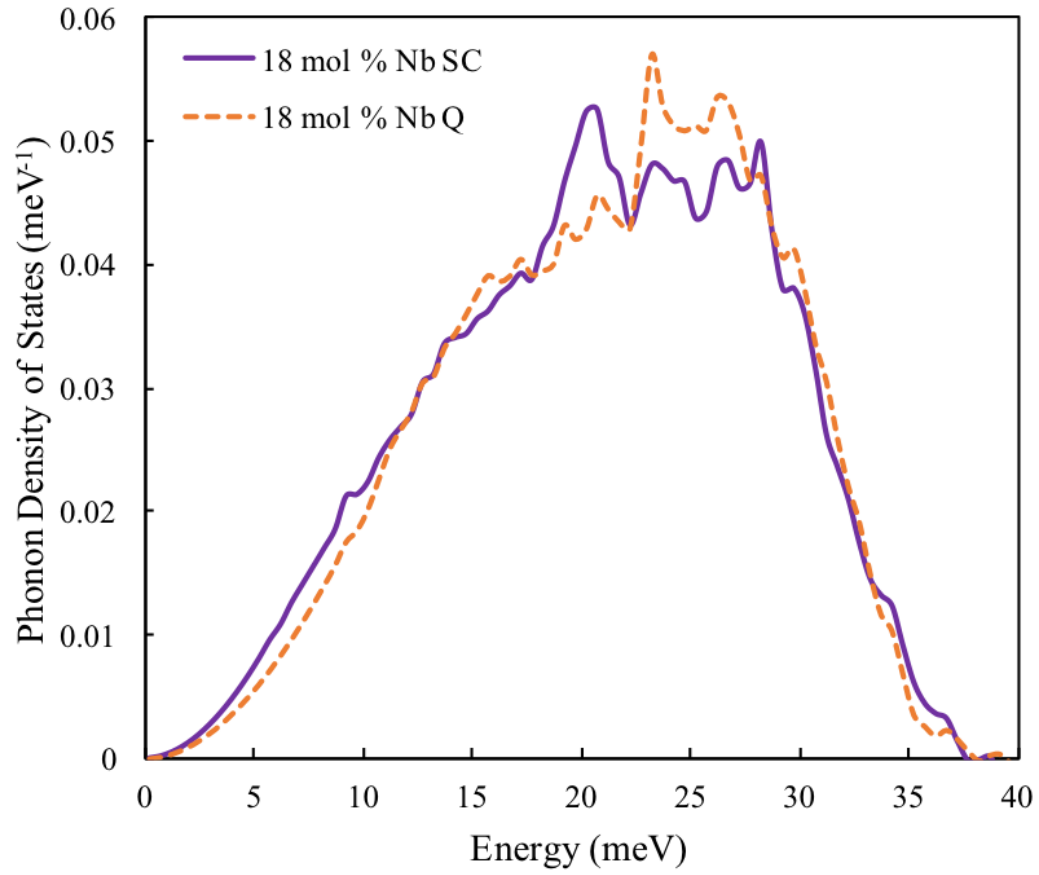


Figure 7.10: Phonon density of states for the Ti-Nb alloy at 18 at. % Nb. The dashed line represents the slow cooled sample while the solid line represents the quenched sample.

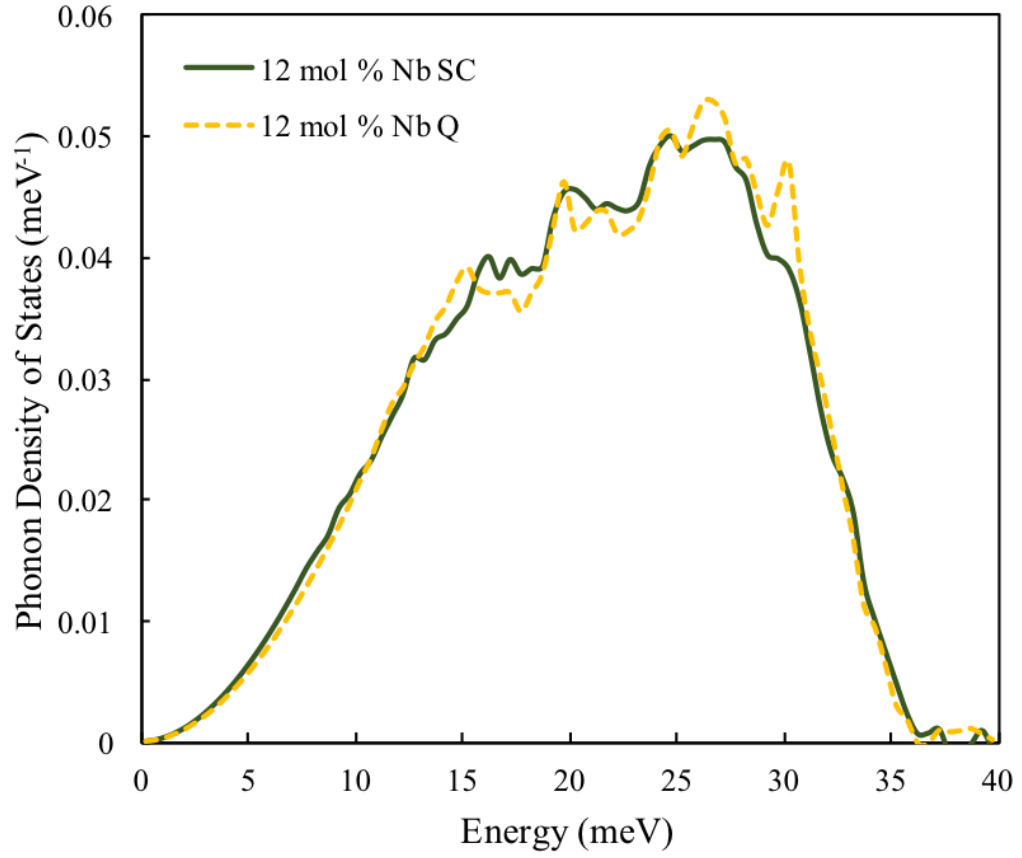


Figure 7.11: Phonon density of states for the Ti-Nb alloy at 12 at. % Nb. The dashed line represents the slow cooled sample while the solid line represents the quenched sample.

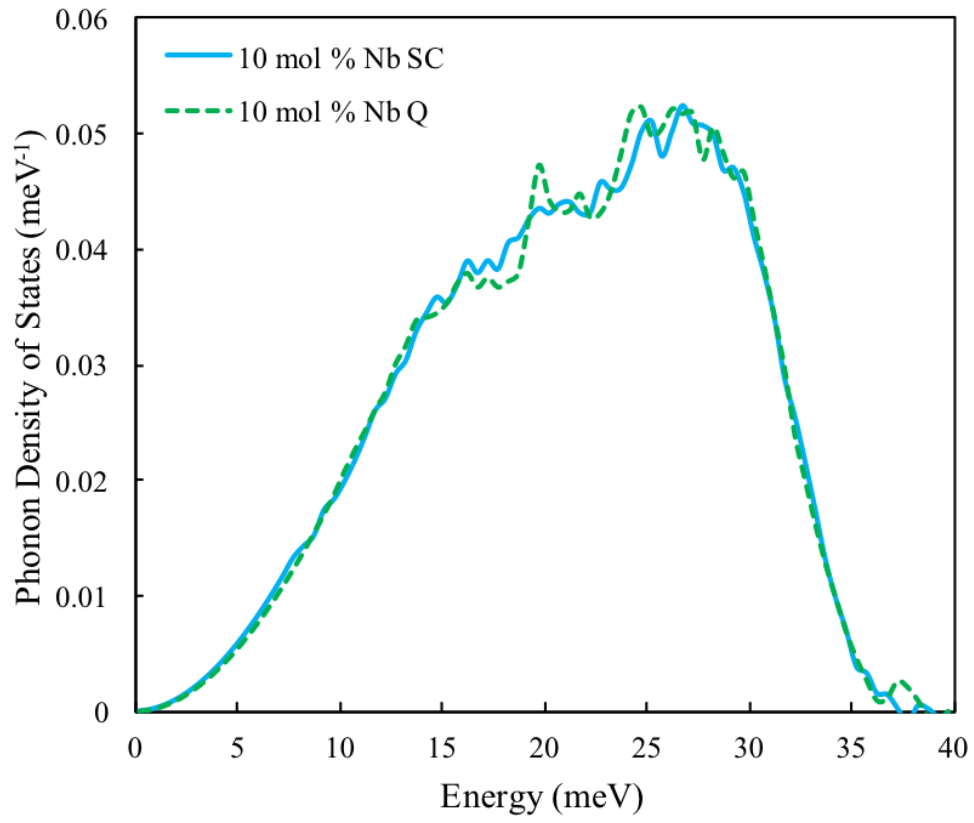


Figure 7.12: Phonon density of states for the Ti-Nb alloy at 10 at. % Nb. The dashed line represents the slow cooled sample while the solid line represents the quenched sample.

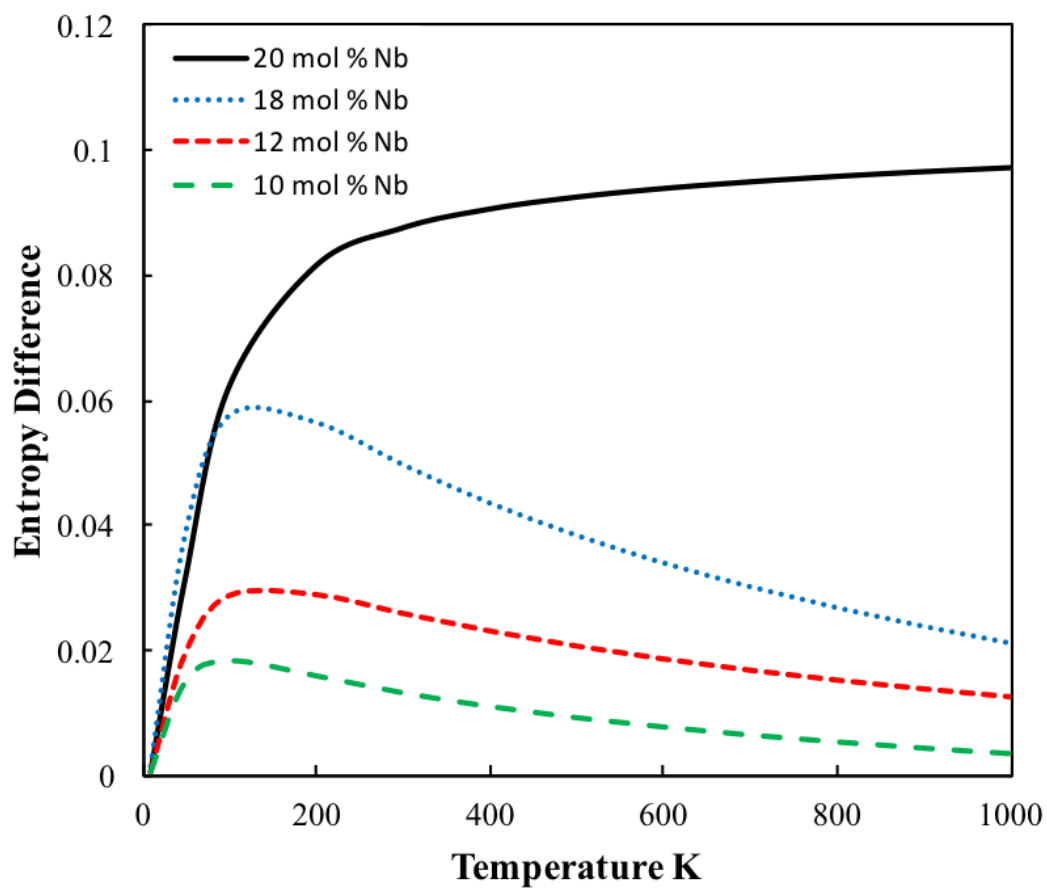


Figure 7.13: Entropy difference between the Ti-Nb alloys with the same alloy composition as a function of temperature.

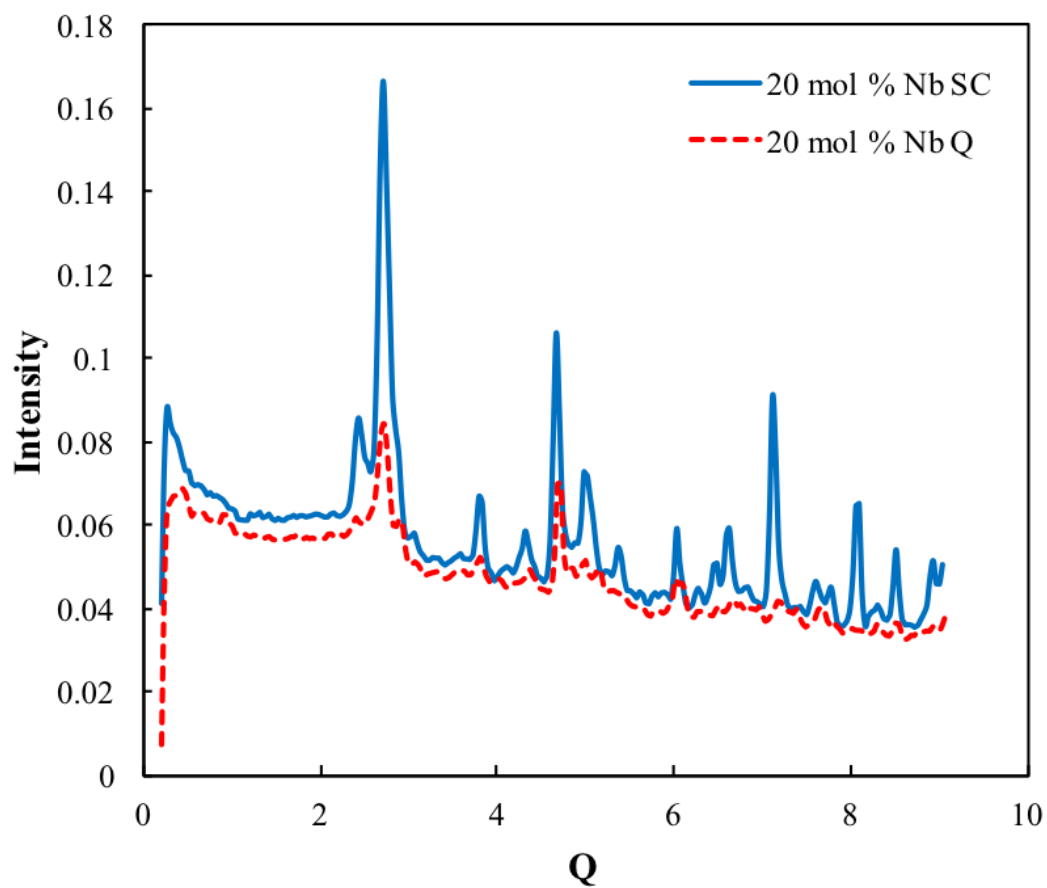


Figure 7.14: Diffraction pattern of the Ti-Nb alloy at 20 at. % Nb. The dashed line represents the slow cooled sample while the solid line represents the quenched sample.

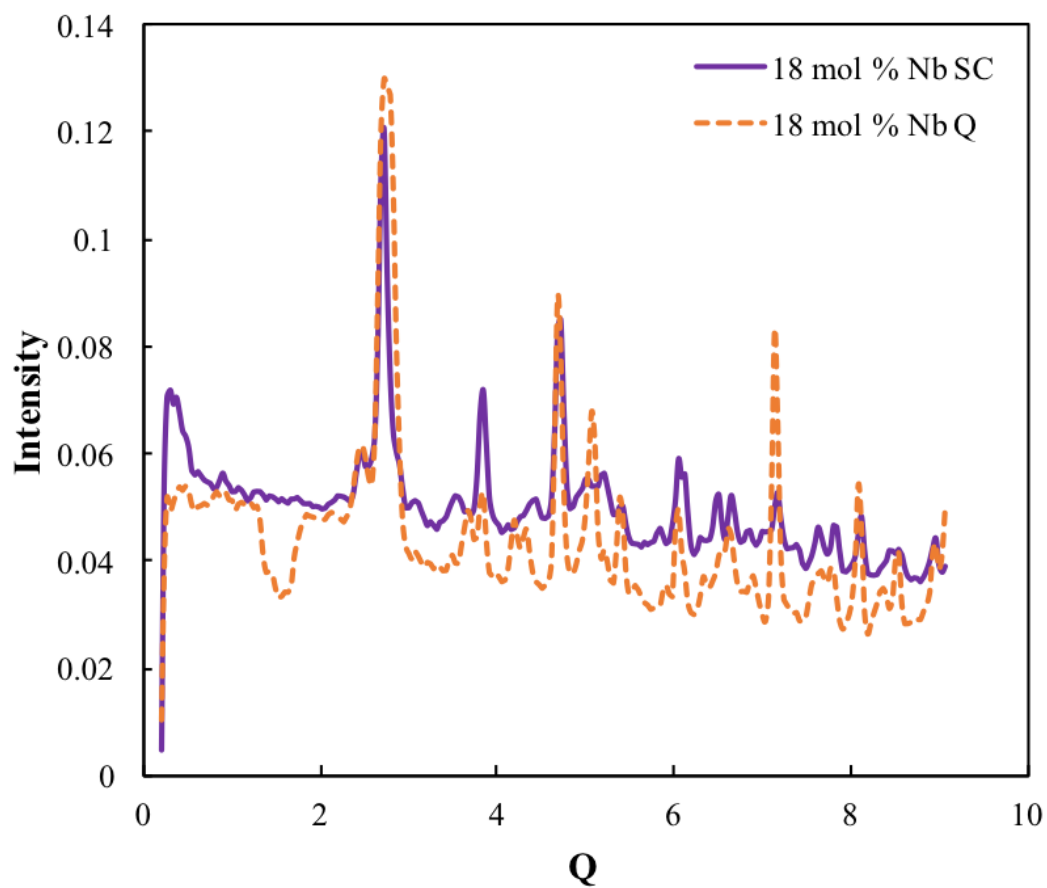


Figure 7.15: Diffraction pattern of the Ti-Nb alloy at 18 at. % Nb. The dashed line represents the slow cooled sample while the solid line represents the quenched sample.

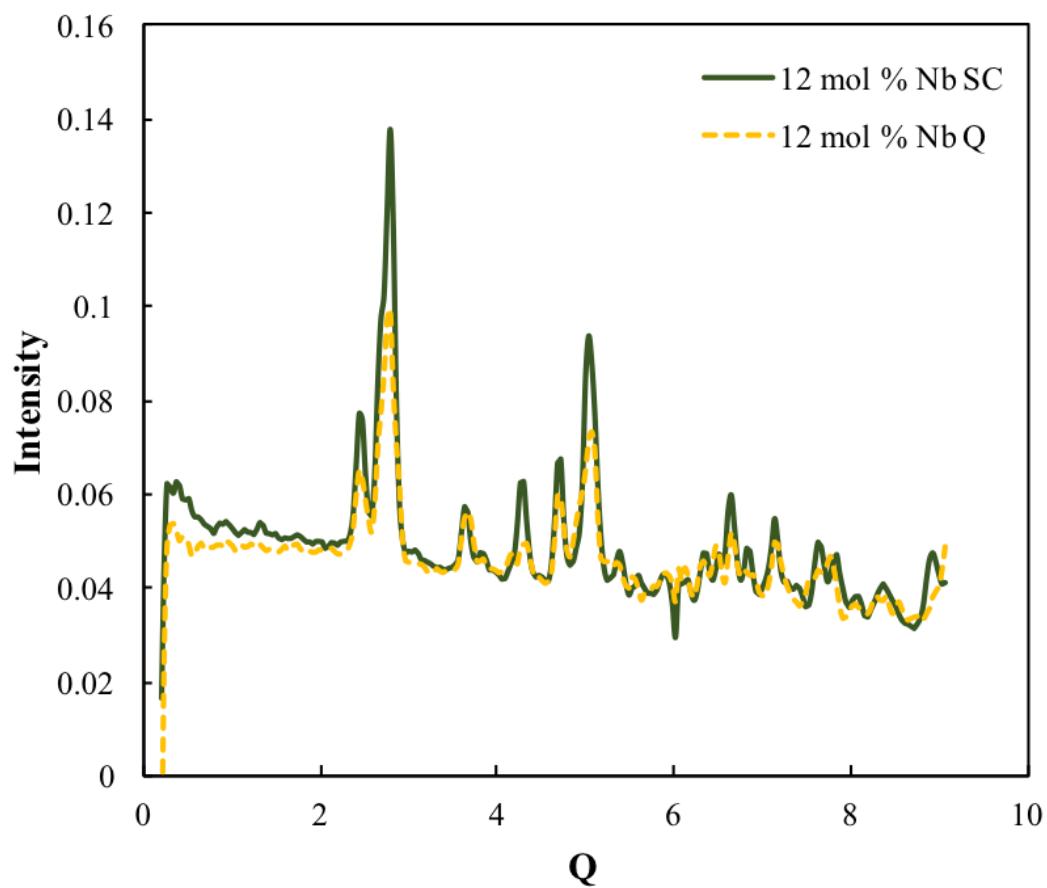


Figure 7.16: Diffraction pattern of the Ti-Nb alloy at 12 at. % Nb. The dashed line represents the slow cooled sample while the solid line represents the quenched sample.

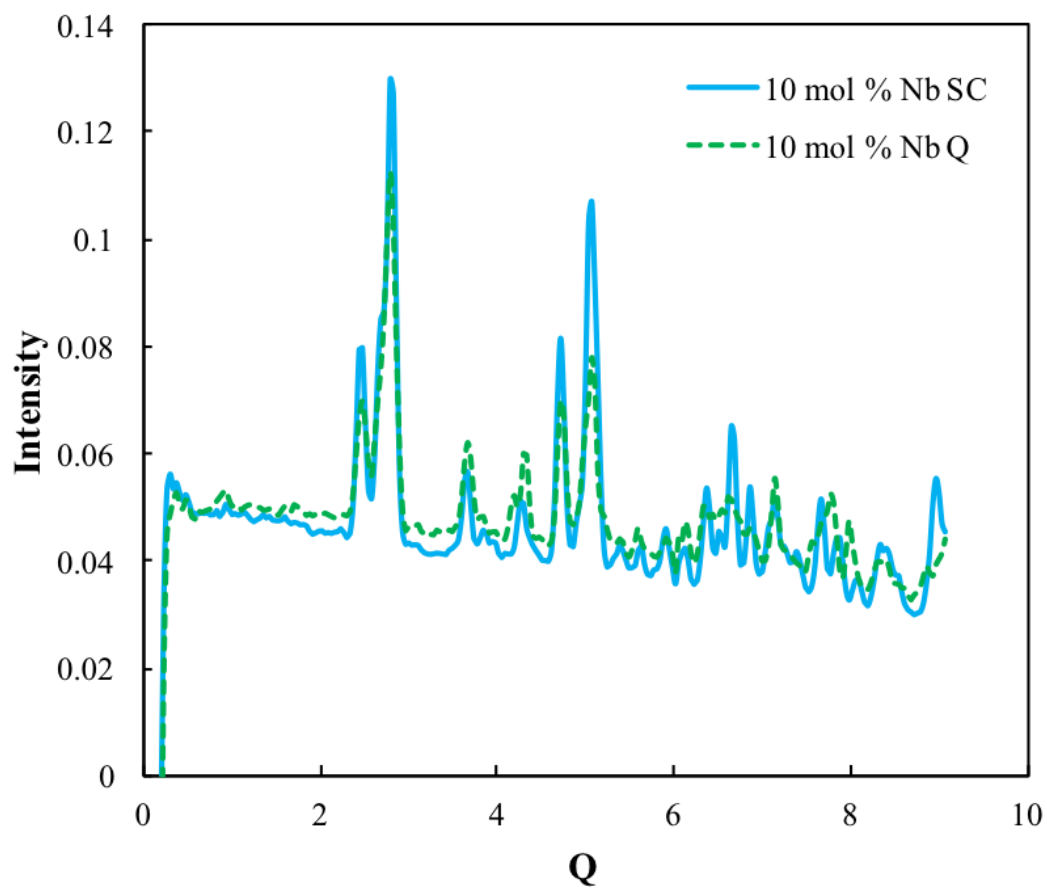


Figure 7.17: Diffraction pattern of the Ti-Nb alloy at 10 at. % Nb. The dashed line represents the slow cooled sample while the solid line represents the quenched sample.